Locating light and heavy atomic column positions with picometer precision using ISTEM

Locating light and heavy atomic column positions with picometer precision using ISTEM

K.H.W. van den Bos[a], F.F. Krause[b], A. Béché[a], J. Verbeeck[a], A. Rosenauer[b], S. Van Aert[a,1,*]

[a]*Electron Microscopy for Materials Science (EMAT), University of Antwerp, Groenenborgerlaan 171, 2020 Antwerp, Belgium*
[b]*Institute for Solid State Physics, University of Bremen, Otto-Hahn-Allee 1, 28359 Bremen, Germany*

Abstract

Recently, imaging scanning transmission electron microscopy (ISTEM) has been proposed as a promising new technique combining the advantages of conventional TEM (CTEM) and STEM [1]. The ability to visualize light and heavy elements together makes it a particularly interesting new, spatially incoherent imaging mode. Here, we evaluate this technique in term of precision with which atomic column locations can be measured. By using statistical parameter estimation theory, we will show that these locations can be accurately measured with a precision in the picometer range. Furthermore, a quantitative comparison is made with HAADF STEM imaging to investigate the advantages of ISTEM.

Keywords: High-resolution (scanning) transmission electron microscopy (HR (S)TEM), Imaging STEM (ISTEM), Quantitative electron microscopy, Statistical parameter estimation theory, Precise determination of atomic column locations

1. Introduction

In the last couple of decades, transmission electron microscopy (TEM) has evolved from a rather qualitative to a quantitative technique. In this process, the introduction of aberration correction [2, 3] and the development of a monochromated electron source [4, 5] has played a major role, since the interpretability of the images improved down to sub-Ångström resolution [6, 7]. This drastic improvement in resolution enables one to visually distinguish atomic columns of crystalline materials when oriented along main zone axis orientations. Moreover, the development of quantitative methods nowadays allows one to precisely extract structural information [8, 9, 10, 11], where the precision corresponds with the variance with which structure parameters can be measured from noisy experimental images. Transmission electron microscopy offers different imaging modes, where conventional TEM (CTEM) and scanning TEM (STEM) are the two most common. In CTEM, an electron plane wave illuminates the specimen followed by an objective lens that forms the image which is recorded in the image plane. In the STEM mode, scattered electrons formed by a focused convergent beam which is scanned over the specimen are collected on an extended disk or annular detector. Recently, Rosenauer et al. [1] proposed a new technique called imaging STEM (ISTEM), which combines STEM illumination with CTEM imaging. This new, spatially incoherent imaging mode is particularly interesting as it provides direct structural images and visualisation of both light and heavy elements. As precise structure determination is essential for understanding the relation between the properties of a nanomaterial and its structure, this new imaging mode is quantitatively evaluated by determining the precision with which individual atomic column positions can be measured. Furthermore, a comparison is made with high angle annular dark field (HAADF) STEM imaging.

The characterisation of materials requires the extraction of atomic column positions with picometer precision, since displacements of atom positions in this range can already alter the material's properties [12, 13]. Model-based quantification offers an effective method to extract structure parameters with a precision several times better than the resolution of the microscope [8, 9, 10, 11]. The precision with which structure parameters can be estimated depends on the signal-to-noise ratio (SNR), which is mainly determined by the incoming electron dose [14] and image distortions [15, 16, 17]. Increasing the incoming electron dose can improve the SNR only to a certain extent, as beam damage must be avoided. By using advanced statistical methods, the incoming electron dose can be tuned to measure structure parameters with a pre-specified precision [10, 14, 18, 19]. Post-processing techniques are capable of reducing the influence of scan noise errors and probe instabilities in STEM imaging [15, 16, 17], while in ISTEM the spatial resolution is not set by the scanning process but by the imaging system. Scan noise and source size broadening hence only influence the electron probe and, as long as the scan raster is fairly homogeneous have no influence at all. Therefore, it is expected that without the use of post-processing techniques, atomic columns can be located more precisely for ISTEM imaging as compared to STEM imaging.

This paper will be organized as follows. Section 2 introduces the material under study together with the experimental conditions and the simulation details. In Section 3, the methodology used for determining the atomic column positions is discussed. Simulated ISTEM images are used in Section 4 to prove the va-

*Corresponding author
Email address: sandra.vanaert@uantwerpen.be (S. Van Aert)
[1]*Phone*: +32 3 2653252
[2]Fax: +32 3 2653318

lidity of the method. In Section 5, the precision with which atomic column positions can experimentally be measured in ISTEM is determined. In addition, a comparison is made with HAADF STEM imaging. Finally, in Section 6, conclusions are drawn.

2. Experiment and simulations

A thin film of $PbTiO_3$ aligned in the [100] zone axis was prepared by focused ion beam (FIB) milling. Ferroelectric structures, like $PbTiO_3$ have been extensively studied because they form the basis of many electronic devices, such as ferroelectric RAMs, sensors and actuators [20, 21, 22, 23]. In this work, the presence of pure oxygen columns along the (100)-planes of this beam stable sample allows us to examine the ability of ISTEM to visualise light atomic columns. HAADF STEM and ISTEM images were simultaneously recorded at the QuAntEm, a double C_s corrected FEI Titan^3, operated at 300 kV with a probe semi-convergence angle of 10 mrad. The spherical aberration of the probe and the image corrector were tuned to 1.2 μm and 1.4 μm, respectively. For HAADF STEM imaging, an ADF detector ranging from 46 to 215 mrad was used. The incident electron dose was $2.5 \cdot 10^5$ electrons per Å^2.

Image simulations of $PbTiO_3$ were performed by using the STEMsim software [24] under the multislice approach with absorptive potentials. This approach has been shown to agree with frozen lattice calculations up to thicknesses of about 20 nm for STEM imaging [25]. In Table 1 the simulation parameters are summarized. The Debye-Waller factors that account for the thermal diffuse scattering were obtained as described in Schowalter et al. [26].

Probe part	Acceleration voltage	300 kV
	Convergence semi-angle	10 mrad
	Defocus	0 nm
	Spherical aberration	90 μm
	Effective source size	0.034 nm
Imaging part	Defocus	−10 nm
	Spherical aberration	10 μm
	Defocus spread	3 nm
STEM detector	inner angle	46 mrad
	outer angle	215 mrad
Structure	Zone axis	[100]
	Supercell periodicity	4×4 unit cells
	Supercell size	15.61×15.61 Å^2
	Supercell mesh	2048×2048
	Specimen thickness	7.8 nm
	Pixel size	0.0156 Å

Table 1: Parameters for the multislice simulations of ISTEM and HAADF STEM images of a $PbTiO_3$ crystal using the STEMsim software.

3. Methodology

In STEM imaging, statistical parameter estimation theory has proven to be an excellent tool to quantitatively extract structure parameters [9]. Here, an experimental image is described by an empirical, parametric model in which the shape of each atomic column is modelled as a Gaussian peak:

$$f_{k,l}(\boldsymbol{\theta}) = \zeta + \sum_{i=1}^{I} \sum_{m_i=1}^{M_i} \eta_{m_i} \exp\left(-\frac{\left(x_k - \beta_{x_{m_i}}\right)^2 + \left(y_l - \beta_{y_{m_i}}\right)^2}{2\rho_i^2} \right) \quad (1)$$

where ζ is a constant background, ρ_i the width of a Gaussian peak of a particular column type i, η_{m_i} the height of the m_i^{th} Gaussian peak, $\beta_{x_{m_i}}$ and $\beta_{y_{m_i}}$ the x- and y-coordinate of the m_i^{th} atomic column, respectively. In the model, the unknown structure parameters are given by the parameter vector: $\boldsymbol{\theta} = (\beta_{x_{1_1}} \cdots \beta_{x_{M_I}}, \beta_{y_{1_1}} \cdots \beta_{y_{M_I}}, \rho_1 \cdots \rho_I, \eta_{1_1} \cdots \eta_{M_I}, \zeta)^T$.

For estimating the parameters $\boldsymbol{\theta}$, use is made of the uniformly weighted least squares estimator:

$$\hat{\boldsymbol{\theta}} = \arg\min_{\mathbf{t}} \sum_{k=1}^{K} \sum_{l=1}^{L} (w_{kl} - f_{kl}(\mathbf{t}))^2 \quad (2)$$

where w_{kl} is the value of the experimental image at the pixel (k, l). For pixel values that are independent and identically normally distributed, the uniformly weighted least squares estimator is equal to the maximum likelihood estimator, which has optimal statistical properties [27]. In electron microscopy, where the recorded intensities are the electron counts, it is reasonable to make the approximation that the image pixel values are normally distributed if the intensity in each pixel is sufficiently high [28].

4. Accuracy of atomic column measurements

The use of the Gaussian model, described in Section 3, on HAADF STEM images is validated by the incoherent image formation process, which is given by the convolution between an object function and the probe intensity [29, 30]. For thicknesses up to 10 nm, the object function is well described by considering only the 1s states of the columns [31]. Furthermore, the detector geometry in HAADF STEM imaging acts as a filter for the highly localized 1s states [30]. Geuens et al. [32] showed that the 1s-state of a column is well approximated by a two-dimensional quadratically normalised Gaussian function. For the estimation of structure parameters, the effect of the probe intensity in C_s corrected microscopes is negligible and can be excluded from the image formation process [33]. Therefore, image intensities can be well described by a superposition of Gaussian peaks [34]. In the ISTEM mode, the effect of the non-1s states on the image formation process is more pronounced as compared to HAADF STEM imaging because of the absence of the filtering effect by the HAADF detector. In order to validate the use of the Gaussian model for extracting column positions, the model is first tested by fitting to simulated images of $PbTiO_3$, see also Fig. 1.

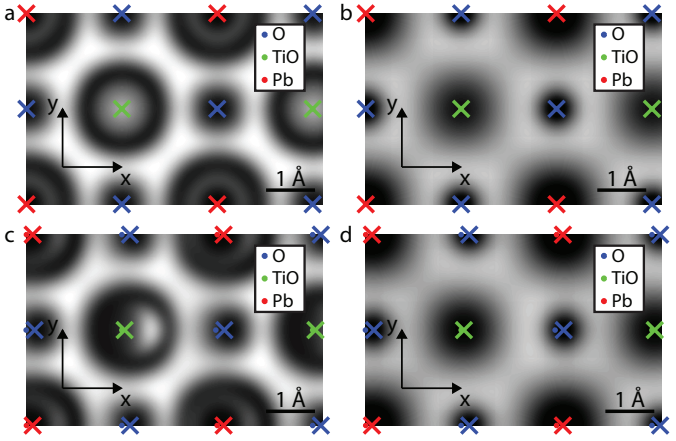

Figure 1: Simulated ISTEM images of $PbTiO_3$ (a) without and (c) with 5.047 mrad tilt together with (b,d) the corresponding fitted models. The true values of the atomic column positions from the input structure of the image simulations are indicated by the dots, the fitted coordinates by the crosses.

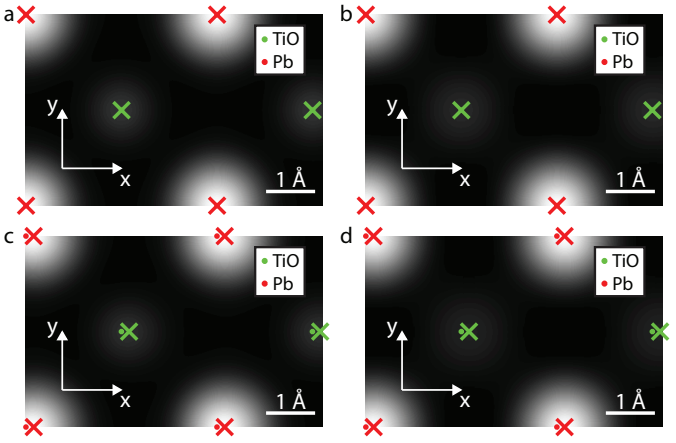

Figure 2: Simulated HAADF STEM images of $PbTiO_3$ (a) without and (c) with 5.047 mrad tilt together with (b,d) the corresponding fitted models. The true values of the atomic column positions from the input structure of the image simulations are indicated by the dots, the fitted coordinates by the crosses.

As opposed to HAADF STEM imaging, the contrast in ISTEM images is dependent on the sample and the microscope settings. With our microscope settings, the atomic column positions are corresponding to the intensity valleys in the images. In the first case, an image simulation of $PbTiO_3$ viewed along the [100]-direction has been used (see Fig. 1(a)). In Fig. 1(b), the fitted, Gaussian model is presented together with the atomic column positions. As can be seen, the model does not fully accurately describe the image intensities. The TiO and Pb columns are described by intensity valleys and hills while they are modelled as drops in intensity. This difference can be explained by the influence of non-1s states on the image formation process which are not modelled. However, the fitted coordinates are perfectly centred on the atomic columns, thus validating the use of the Gaussian model for determining atomic column locations. The effectiveness of the model can be explained by the shape of the columns in the image. Despite the influence of the non-1s states, their intensity profiles are mainly described by a drop in intensity. Furthermore, these profiles are circularly symmetric. Therefore, any circular shaped model, like the Gaussian one, will most likely find the column locations.

In order to test the model on a non-symmetric case, an image simulation of a $PbTiO_3$ crystal tilted by 5.047 mrad in the x-direction has been evaluated (see Fig. 1(c)). In this case, the (001) beam is strongly excited and the Laue circle runs through the (000) and (002) beams, giving the smallest sample tilt that results in a visible asymmetry of the diffraction pattern [35, 36]. The fitted coordinates obtained from the Gaussian model are shifted along the x-axis with respect to the true values of the atomic column positions (see Table 2). Here, the top-most atom of each column was taken as a reference. A closer look at the image shows that the fitted coordinates are centred on the intensity valleys, indicating that the fitting procedure works as expected. Similarly, Zhou et al. [36] showed that in HAADF STEM imaging tilt induces an intensity shift in the formed images which is dependent on tilt angle, sample thickness and probe convergence semi-angle. In order to compare the effects of tilt between ISTEM and HAADF STEM imaging, HAADF STEM image simulations of a non-tilted and a 5.047 mrad tilted $PbTiO_3$ crystal have been quantified by the Gaussian model (see also Fig. 2). In the absence of sample tilt, the fitted coordinates are exactly the same as the true values. As is presented in Table 2, for sample tilt the fitted coordinates are shifted with respect to the true values of the atomic column positions by approximately the same value for the two column types. Appendix A shows that by changing to a more conventional probe convergence semi-angle of 21 mrad in HAADF STEM imaging, the measured shift remains approximately the same for the different column types. These results suggest that for HAADF STEM imaging tilt induces an overall translation of the image. This is, however, not the case in ISTEM imaging as Table 2 points out. Despite the lower shift introduced by tilt, the shift is column type dependent and will therefore depict a deformed unit cell. This difference is probably caused by the presence of non-1s states in the ISTEM image formation process, as the presence of these states also seem to affect negative Cs TEM images (see Appendix B). The development of a model that also considers these non-1s states will most likely visually describe the pixel values better. It is, however, expected that only when the effect of tilt of the electron beam is included in such a model, atomic column position measurements will improve. Despite the disadvantage of a column type dependent shift, sample tilt can be identified more easily from

Column	ISTEM Accuracy (pm)	HAADF STEM Accuracy (pm)
O	15.59	Not possible
TiO	5.72	14.86
Pb	12.92	15.69

Table 2: The absolute distance between the x-coordinates of the fitted coordinates and the true values of the atomic columns in the simulated images of a $PbTiO_3$ crystal tilted by 5.047 mrad.

ISTEM images as compared to HAADF STEM images because the intensity distribution of columns becomes non-symmetric. Still, one should keep in mind that column locations are sensitive to sample tilt when using them for applications such as strain mapping [36].

5. Precision of atomic column measurements

As is demonstrated in Section 4, statistical parameter estimation theory is capable of extracting atomic column positions with a high accuracy from ISTEM images. In order to determine how precise atomic column positions can be measured, an experimental ISTEM image of $PbTiO_3$ has been evaluated (see Fig. 3(a)). For the extraction of the positions, the Gaussian model (Eq. 1) has been fitted by fixing the background value to the maximum pixel value in order to ensure that all oxygen columns are found (see Fig. 3(b)). Next, the lattice parameter is determined by measuring the distance between neighbouring columns of the same type. In this procedure, columns are grouped in pairs along the horizontal direction to ensure that measurements are independent of each other. The precision is measured in terms of the standard deviation on the measured lattice parameter assuming a fully periodic structure. In order to compare the results, 95% confidence intervals are calculated using the following expression:

$$\sqrt{\frac{(n-1)s^2}{\chi^2_{n-1,0.025}}} \leq \sigma \leq \sqrt{\frac{(n-1)s^2}{\chi^2_{n-1,0.975}}} \qquad (3)$$

with s^2 the sample variance and $\chi^2_{n-1,\alpha}$ the α quantile of the χ^2 distribution with $n-1$ degrees of freedom. The results presented in Table 3 show that all the different column positions can be measured with a precision in the picometer range. The worse precision of the O columns can be explained by their low atomic number, which results in a less pronounced column intensity profile. The precision of the TiO columns is slightly better as compared to the Pb columns.

In order to compare these results to HAADF STEM imaging, a simultaneously recorded image of $PbTiO_3$ with the same incoming electron dose has been evaluated (see Fig. 3(c)). The fitted Gaussian model, presented in Fig. 3(d), has been used to extract the atomic column positions. Similar as before, the precision on the lattice parameters has been measured by grouping columns of the same type in the x-direction together (see Table 3). The major advantage of ISTEM is, as expected, the visualisation of light atoms. In HAADF STEM imaging the intensity

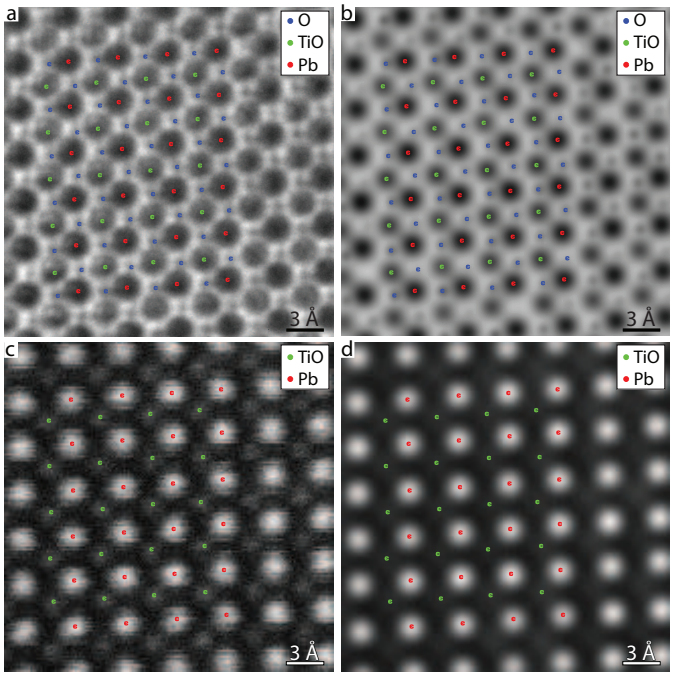

Figure 3: An experimental (a) ISTEM and (c) HAADF STEM image of $PbTiO_3$ with (b,d) the corresponding fitted models. The estimated column positions are shown as an overlay.

contributions of these columns cannot be distinguished from the noise level. A comparison of the other, more heavy, columns, shows that the precision with which positions are measured is better in ISTEM as compared to HAADF STEM.

For investigating the mechanisms that determine the precision, 100 noise realisations of simulated ISTEM and HAADF STEM images are evaluated. Here, only image, or shot, noise is modelled by using random Poisson distributed pixel values. Simulation parameters as summarized in Table 1 are used with an incident electron dose equal to the experimental dose, $2.5 \cdot 10^5$ electrons per Å^2. Similar as in the experimental image, the precision is measured in terms of the standard deviation on the measured lattice parameters. Here, the two most central neighbouring columns of the same type are grouped together to calculate the lattice parameter. Table 4 shows the measured precision with the 95% confidence interval obtained by Eq. 3. For both imaging techniques, the precision is an order of magnitude smaller as compared to the experimentally measured precision. Appendix A shows that the influence of the probe convergence semi-angle in HAADF STEM imaging on the precision

Column	ISTEM Precision (pm)	HAADF STEM Precision (pm)
O - O	6.89 (*5.30 – 9.84*)	Not possible
TiO - TiO	3.44 (*2.37 – 6.29*)	10.81 (*7.43 – 19.73*)
Pb - Pb	5.17 (*3.66 – 8.77*)	6.01 (*4.26 – 10.20*)

Table 3: The experimental precision on the distance between neighbouring columns of the same type. The 95% confidence intervals are given in brackets.

Column	ISTEM Precision (pm)	HAADF STEM Precision (pm)
O - O	0.12 (*0.10 – 0.14*)	Not possible
TiO - TiO	0.13 (*0.11 – 0.16*)	0.76 (*0.67 – 0.88*)
Pb - Pb	0.11 (*0.10 – 0.13*)	0.32 (*0.28 – 0.37*)

Table 4: The attainable precision with which column positions can be located when only Poisson noise is present. The 95% confidence intervals are given in brackets.

is small, indicating that the use of the non-conventional probe convergence semi-angle of 10 mrad will most likely not affect the measured precision. The large difference between the values obtained from the simulations and the experiment points out that the presence of image distortions, sample drift and local varying crystal orientations in the experimental image mainly determines the precision of the measured column locations. For ISTEM this difference suggests that the integration of all probe positions does not compensate for all these effects. However, the robustness of ISTEM to probe instabilities and scan noise errors allows more precise measures for column locations as compared to HAADF STEM imaging, with the added benefit of allowing to measure also the light atomic columns. Furthermore, the results of Table 4 suggest that in the ideal case when only image, or shot, noise is present, atomic column locations can be measured with a better precision from ISTEM images as compared to HAADF STEM images.

6. Conclusions

In this paper, we propose a model-based parameter estimation framework for extracting atomic column locations from ISTEM images. In this framework, image intensities are modelled as a superposition of Gaussian peaks. Despite the complex image formation process in ISTEM imaging which cannot be fully accurately described by this relative simple model, it is still possible to accurately measure column locations in the absence of sample tilt. Similar as in HAADF STEM imaging, tilt induces a bias in the estimated column locations. In ISTEM imaging this bias is column type dependent and can result in the depiction of a deformed unit cell, while in HAADF STEM imaging this will not occur as the bias is approximately the same for different column types. Despite this disadvantage of ISTEM imaging, sample tilt can be more easily identified as compared to HAADF STEM imaging since the intensity distribution of the columns becomes non-symmetric. From experimental images it has been demonstrated that both light and heavy atomic column positions can be measured with picometer precision from ISTEM images. Therefore, this imaging mode is extremely useful for the characterisation of systems composed out of a mixture of light and heavy atoms, such as oxides and perovskites. Furthermore, ISTEM is capable of measuring column locations with a better precision as compared to HAADF STEM imaging. Because of these abilities we expect that in the near future ISTEM will become an important imaging mode to retrieve structural parameters in a quantitative manner.

7. Acknowledgements

The authors acknowledge financial support from the Research Foundation Flanders (FWO, Belgium) through project fundings (G.0374.13N, G.0368.15N, G.0369.15N), and by a Ph.D. grant to K.H.W. van den Bos. The research leading to these results has received funding from the Deutsche Forschungsgemeinschaft under Contract No. RO 2057/4-2 and the European Union Seventh Framework Programme under Grant Agreement 312483 - ESTEEM2. We thank Prof. G. Koster from the University of Twente for kindly providing us with the $PbTiO_3$ test sample.

Appendix A. Influence of the convergence semi-angle on estimated column locations

In HAADF STEM imaging, the conventional applied probe convergence semi-angle is in the 20 mrad range, while the experimentally used 10 mrad is optimal for ISTEM imaging. For a fair comparison between HAADF STEM and ISTEM, the effect of the probe convergence semi-angle on the estimated accuracy and precision with which atomic columns can be located is evaluated by using image simulations of $PbTiO_3$ (see Fig. A.1). Simulation settings as summarized in Table 1 are used in which the probe convergence semi-angle is set to 21 mrad. Similar as in section 4, the accuracy of the estimated column locations is investigated for a case without sample tilt and one where the $PbTiO_3$ crystal is tilted by 5.047 mrad along the x-direction. The Gaussian model, described in Section 3 has been used to extract the atomic column positions. For the case without sample tilt, the fitted coordinates of the atomic columns are exactly the same as the true values, given by the top-most atoms. When sample tilt is present, the fitted coordinates shift with respect to the true values (see Table A.1). The results for a probe convergence semi-angle of 10 mrad, as presented in section 4, are shown in Table A.1 for comparison. For both probe convergence semi-angles, the difference between the fitted x-coordinates and the true values is approximately the same for the different column types.

In order to test the influence of the probe convergence semi-angle on the precision with which atomic column locations can be estimated, 100 noise realizations of the simulated HAADF STEM image of $PbTiO_3$ without sample tilt have been examined. Image, or shot, noise is modelled by using random Poisson distributed pixel values for an incident electron dose of

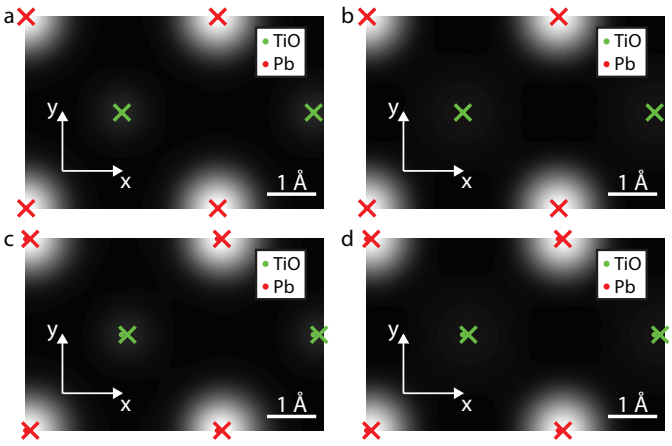

Figure A.1: Simulated HAADF STEM images with a probe convergence semi-angle of 21 mrad of $PbTiO_3$ (a) without and (c) with 5.047 mrad sample tilt together with (b,d) the corresponding fitted models. The true values of the atomic column positions from the input structure of the image simulations are indicated by the dots, the fitted coordinates by the crosses.

Column	α = 21 mrad Accuracy (pm)	α = 10 mrad Accuracy (pm)
TiO	9.85	14.86
Pb	9.56	15.69

Table A.1: The effect of the probe convergence semi-angle on the estimated coordinates in HAADF STEM simulated images of $PbTiO_3$ crystal tilted by 5.047 mrad in the x-direction. The distance between the x-coordinates of the fitted coordinates and the true values is given for the different atomic column types.

Column	α = 21 mrad Precision (pm)	α = 10 mrad Precision (pm)
TiO	1.05 (*0.92 – 1.21*)	0.76 (*0.67 – 0.88*)
Pb	0.34 (*0.30 – 0.40*)	0.32 (*0.28 – 0.37*)

Table A.2: The precision with which the x-coordinates of the atomic columns are determined from HAADF STEM image simulations for different probe convergence semi-angles. The 95% confidence intervals are given in brackets.

$2.5 \cdot 10^5$ electrons per Å^2. Image distortions are not modelled. Similar as in section 5, the precision is measured in terms of the standard deviation on the estimated lattice parameters by grouping neighbouring columns of the same type together. For each column type, the two most central columns in the simulated image are used for calculating the lattice parameter. Table A.2 shows the measured precision with the 95% confidence intervals obtained by using Eq. 3. The results for a probe convergence semi-angle of 10 mrad, as presented in section 5, are also shown in Table A.2 for comparison. The standard deviation of the estimated column location is slightly larger in the 21 mrad case. However, compared to the experimental measured precision it is still orders of magnitude smaller (see Table 3). Therefore, it is expected that the influence of the probe semi-convergence angle is negligible.

Appendix B. Influence of sample tilt in negative Cs imaging

As is shown in section 4, sample tilt induces in both ISTEM and HAADF STEM imaging a translation of the image intensities. While in HAADF STEM imaging this translation is approximately uniform for different column type, it is column type dependent in ISTEM imaging. The main difference between both imaging techniques is the presence of non-1s states in the image formation process of ISTEM imaging. In order to verify whether these states can explain the column type dependent shift, negative Cs TEM image simulations of a $PbTiO_3$ crystal are evaluated (see Fig. A.2). In this imaging technique non-1s states may also influence the formed images. The simulation parameters as summarized in Table 1 are used together with plane wave illumination and an imaging part with a defocus of 2 nm and spherical aberration of -2 μm. Similar as in section 4, the accuracy of the estimated column locations is investigated for a case without sample tilt and one where the $PbTiO_3$ crystal is tilted by 5.047 mrad along the x-direction. The Gaussian model, described in Section 3 has been used to extract the atomic column positions. Similar as for ISTEM,

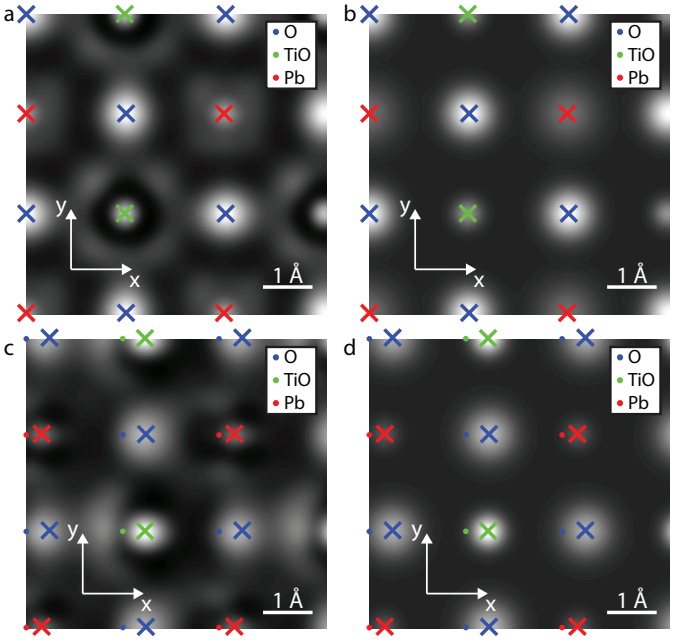

Figure A.2: Simulated negative Cs TEM images of $PbTiO_3$ (a) without and (c) with 5.047 mrad sample tilt together with (b,d) the corresponding fitted models. The true values of the atomic column positions from the input structure of the image simulations are indicated by the dots, the fitted coordinates by the crosses.

the model does not adequately describe the complex image intensity distribution of each column. However, for the untilted case the fitted coordinates of the atomic columns are exactly the same as the true values, given by the top-most atoms. Therefore, this result validate the use of the Gaussian model to extract atomic column locations. When sample tilt is present, the fitted coordinates shift with respect to the true values (see Table A.3). The results for ISTEM imaging, as presented in section 4, are shown for comparison. The values in Table A.3 indicate that negative Cs imaging is more sensitive to sample tilt in comparison with ISTEM imaging. Similar as in ISTEM imaging, the shift of the fitted coordinates with respect to the true values depends in negative Cs imaging on the column type. Therefore, these results seem to confirm that the presence of non-1s states in the image formation process may cause a column type dependent translation of the image intensities when tilt is present.

Column	negative Cs TEM Accuracy (pm)	ISTEM Accuracy (pm)
O	47.06	15.59
TiO	44.86	5.72
Pb	31.05	12.92

Table A.3: The absolute distance between the x-coordinates of the fitted coordinates and the true values of the atomic columns in the simulated images of a $PbTiO_3$ crystal tilted by 5.047 mrad.

References

[1] A. Rosenauer, F. F. Krause, K. Müller, M. Schowalter, T. Mehrtens, Conventional transmission electron microscopy imaging beyond the diffrac-

tion and information limits, Physical Review Letters 113 (9) (2014) 096101.
[2] H. Rose, Elektronenoptische aplanate, Optik 34 (285) (1971) 12.
[3] H. Rose, Outline of a spherically corrected semi-aplanatic medium-voltage transmission electron-microscope, Optik 85 (1) (1990) 19–24.
[4] H. W. Mook, P. Kruit, Optics and design of the fringe field monochromator for a schottky field emission gun, Nuclear Instruments and Methods in Physics Research Section A 427 (1) (1999) 109–120.
[5] O. L. Krivanek, J. P. Ursin, N. J. Bacon, G. J. Corbin, N. Dellby, P. Hrncirik, M. F. Murfitt, C. S. Own, Z. S. Szilagyi, High-energy-resolution monochromator for aberration-corrected scanning transmission electron microscopy/electron energy-loss spectroscopy, Philosophical Transactions of the Royal Society of London A: Mathematical, Physical and Engineering Sciences 367 (1903) (2009) 3683–3697.
[6] K. W. Urban, Studying atomic structures by aberration-corrected transmission electron microscopy, Science 321 (5888) (2008) 506–510.
[7] R. Erni, M. D. Rossell, C. Kisielowski, U. Dahmen, Atomic-resolution imaging with a sub-50-pm electron probe, Physical Review Letters 102 (9) (2009) 096101.
[8] S. Bals, S. Van Aert, G. Van Tendeloo, D. Ávila-Brande, Statistical estimation of atomic positions from exit wave reconstruction with a precision in the picometer range, Physical Review Letters 96 (9) (2006) 096106.
[9] S. Van Aert, J. Verbeeck, R. Erni, S. Bals, M. Luysberg, D. Van Dyck, G. Van Tendeloo, Quantitative atomic resolution mapping using high-angle annular dark field scanning transmission electron microscopy, Ultramicroscopy 109 (10) (2009) 1236–1244.
[10] A. J. den Dekker, J. Gonnissen, A. De Backer, J. Sijbers, S. Van Aert, Estimation of unknown structure parameters from high-resolution (S)TEM images: What are the limits?, Ultramicroscopy 134 (2013) 34–43.
[11] S. Van Aert, A. De Backer, G. T. Martinez, A. J. den Dekker, D. Van Dyck, S. Bals, G. Van Tendeloo, Advanced electron crystallography through model-based imaging, IUCrJ 3 (3) (2016) 71–83.
[12] D. A. Muller, Why changes in bond lengths and cohesion lead to core-level shifts in metals, and consequences for the spatial difference method, Ultramicroscopy 78 (1) (1999) 163–174.
[13] C. Kisielowski, E. Principe, B. Freitag, D. Hubert, Benefits of microscopy with super resolution, Physica B 308 (2001) 1090–1096.
[14] S. Van Aert, D. Van Dyck, A. J. den Dekker, Resolution of coherent and incoherent imaging systems reconsidered - classical criteria and a statistical alternative, Optics Express 14 (9) (2006) 3830–3839.
[15] L. Jones, P. D. Nellist, Identifying and correcting scan noise and drift in the scanning transmission electron microscope, Microscopy and Microanalysis 19 (4) (2013) 1050–1060.
[16] X. Sang, J. M. LeBeau, Revolving scanning transmission electron microscopy: correcting sample drift distortion without prior knowledge, Ultramicroscopy 138 (2014) 28–35.
[17] L. Jones, H. Yang, T. J. Pennycook, M. S. J. Marshall, S. Van Aert, N. D. Browning, M. R. Castell, P. D. Nellist, Smart Align–a new tool for robust non-rigid registration of scanning microscope data, Advanced Structural and Chemical Imaging 1 (8) (2015) 1–16.
[18] J. Gonnissen, A. De Backer, A. J. Den Dekker, G. T. Martinez, A. Rosenauer, J. Sijbers, S. Van Aert, Optimal experimental design for the detection of light atoms from high-resolution scanning transmission electron microscopy images, Applied Physics Letters 105 (6) (2014) 063116.
[19] A. De Backer, A. De wael, J. Gonnissen, S. Van Aert, Optimal experimental design for nano-particle atom-counting from high-resolution STEM images, Ultramicroscopy 151 (2015) 46–55.
[20] M. Okuyama, Y. Hamakawa, Preparation and basic properties of $PbTiO_3$ ferroelectric thin films and their device applications, Ferroelectrics 63 (1) (1985) 243–252.
[21] J. F. Scott, Applications of modern ferroelectrics, Science 315 (5814) (2007) 954–959.
[22] S. Zhang, F. Li, High performance ferroelectric relaxor-$PbTiO_3$ single crystals: Status and perspective, Journal of Applied Physics 111 (3) (2012) 031301.
[23] R. Egoavil, H. Tan, J. Verbeeck, S. Bals, B. Smith, B. Kuiper, G. Rijnders, G. Koster, G. Van Tendeloo, Atomic scale investigation of a $PbTiO_3/SrRuO_3/DyScO_3$ heterostructure, Applied Physics Letters 102 (22) (2013) 223106.
[24] A. Rosenauer, M. Schowalter, STEMSIM-a new software tool for simulation of STEM HAADF" Z-contrast imaging, in: Microscopy of Semiconducting Materials 2007, Springer, 2008, pp. 170–172.
[25] A. Rosenauer, M. Schowalter, J. T. Titantah, D. Lamoen, An emission-potential multislice approximation to simulate thermal diffuse scattering in high-resolution transmission electron microscopy, Ultramicroscopy 108 (12) (2008) 1504–1513.
[26] M. Schowalter, A. Rosenauer, J. T. Titantah, D. Lamoen, Computation and parametrization of the temperature dependence of debye–waller factors for group IV, III–V and II–VI semiconductors, Acta Crystallographica Section A 65 (1) (2009) 5–17.
[27] A. J. Den Dekker, S. Van Aert, A. Van den Bos, D. Van Dyck, Maximum likelihood estimation of structure parameters from high resolution electron microscopy images. Part I: a theoretical framework, Ultramicroscopy 104 (2) (2005) 83–106.
[28] M. A. O. Miedema, A. Van den Bos, A. H. Buist, Experimental design of exit wave reconstruction from a transmission electron microscope defocus series, IEEE Transactions on Instrumentation and Measurement 43 (2) (1994) 181–186.
[29] S. J. Pennycook, D. E. Jesson, High-resolution Z-contrast imaging of crystals, Ultramicroscopy 37 (1) (1991) 14–38.
[30] P. D. Nellist, S. J. Pennycook, Incoherent imaging using dynamically scattered coherent electrons, Ultramicroscopy 78 (1) (1999) 111–124.
[31] J. Broeckx, M. Op de Beeck, D. Van Dyck, A useful approximation of the exit wave function in coherent STEM, Ultramicroscopy 60 (1) (1995) 71–80.
[32] P. Geuens, D. Van Dyck, The S-state model: a work horse for HRTEM, Ultramicroscopy 93 (3) (2002) 179–198.
[33] G. T. Martinez, A. De Backer, A. Rosenauer, J. Verbeeck, S. Van Aert, The effect of probe inaccuracies on the quantitative model-based analysis of high angle annular dark field scanning transmission electron microscopy images, Micron 63 (2014) 57–63.
[34] A. De Backer, G. T. Martinez, K. E. MacArthur, L. Jones, A. Béché, P. D. Nellist, S. Van Aert, Dose limited reliability of quantitative annular dark field scanning transmission electron microscopy for nano-particle atom-counting, Ultramicroscopy 151 (2015) 56–61.
[35] A. Rosenauer, Transmission electron microscopy of semiconductor nanostructures: an analysis of composition and strain state, Vol. 182, Springer Science & Business Media, 2003.
[36] D. Zhou, K. Müller-Caspary, W. Sigle, F. F. Krause, A. Rosenauer, P. A. van Aken, Sample tilt effects on atom column position determination in ABF–STEM imaging, Ultramicroscopy 160 (2016) 110–117.